

Communication

Self-Assembled $\text{La}_{0.67}\text{Sr}_{0.33}\text{MnO}_3\text{:CeO}_2$ Vertically Aligned Nanocomposite Thin Films on Flexible Mica

Hongxia Tian ¹, Xiong Zhang ², Abdullah Alodhayb ³ , Feng Wang ¹, Jie Jian ^{4,*} and Jijie Huang ^{2,*}

¹ Institute of Mold Technology, Changzhou Vocational Institute of Mechatronic Technology, Changzhou 213164, China

² School of Materials, Shenzhen Campus of Sun Yat-sen University, Shenzhen 518107, China

³ Department of Physics and Astronomy, College of Science, King Saud University, Riyadh 11451, Saudi Arabia

⁴ Institute of Special Environments Physical Sciences, Harbin Institute of Technology (Shenzhen), Shenzhen 518055, China

* Correspondence: jianjie@hit.edu.cn (J.J.); huangjj83@mail.sysu.edu.cn (J.H.)

Abstract: Vertically aligned nanocomposite (VAN) thin film has attracted tremendous research interests owing to its multifunctionality, enhanced physical properties and multi-field coupling. However, VAN has rarely been demonstrated in flexible form, which hinders its further application in flexible devices. In this work, $\text{La}_{0.67}\text{Sr}_{0.33}\text{MnO}_3\text{-CeO}_2$ (LC) VAN film has been deposited on flexible mica with or without a buffer layer. The LC nanocomposite films show high quality following textured growth and form a typical, vertically aligned nanostructure. Magnetic, transport and magnetoresistance properties have been explored for flexible nanocomposite thin films. Furthermore, flexible LC films maintain their properties after numerous mechanical bending tests, presenting promising future applications in flexible electronics and spintronics.

Keywords: nanocomposite thin film; flexible; mica; magnetoresistance



Citation: Tian, H.; Zhang, X.; Alodhayb, A.; Wang, F.; Jian, J.; Huang, J. Self-Assembled $\text{La}_{0.67}\text{Sr}_{0.33}\text{MnO}_3\text{:CeO}_2$ Vertically Aligned Nanocomposite Thin Films on Flexible Mica. *Crystals* **2023**, *13*, 1595. <https://doi.org/10.3390/cryst13111595>

Academic Editor: Serguei Petrovich Palto

Received: 18 September 2023

Revised: 23 October 2023

Accepted: 16 November 2023

Published: 17 November 2023



Copyright: © 2023 by the authors. Licensee MDPI, Basel, Switzerland. This article is an open access article distributed under the terms and conditions of the Creative Commons Attribution (CC BY) license (<https://creativecommons.org/licenses/by/4.0/>).

1. Introduction

Functional oxide thin films have great potential in electronic and spintronic device applications, owing to their rich physical properties and couplings, which involve ferroelectrics, magnetism, dielectrics, photonics, superconductors, etc. [1]. In addition to the conventional one-phase oxide thin films, vertically aligned nanocomposite (VAN) thin films have aroused tremendous research interests because of their unique nanostructure, as well as multifunctionality and multi-field coupling induced by the vertical heterointerface [2–4]. For example, multiferroicity has been discovered in very limited single-phase materials, such as BiFeO_3 (BFO) [5,6] and TbMnO_3 (TMO) [7,8]. On the other hand, nanocomposite thin film provides a perfect platform to design multiferroic materials by growing ferromagnetic (antiferromagnetic) and ferroelectric phases into one layer [9,10]. Furthermore, enhanced ferroelectricity [11], perpendicular exchange bias [12], tunable low-field magnetoresistance (LFMR) [13] and novel electrical/ionic properties [14] have also been explored in nanocomposite thin films. To date, different VAN systems have been investigated, such as oxide–oxide [2,3], metal–oxide [15], metal–nitride [16], as well as the recently developed oxide–alloy [17] systems.

To obtain VAN thin films, single-crystal substrates with certain lattice parameters should be selected. The most used ones include SrTiO_3 (STO), LaAlO_3 (LAO), MgO , etc. [2–4]. Considering their potential in Si-based devices, VANs have also been integrated on Si wafers with sets of buffer layers to overcome lattice mismatch and possible interdiffusion [18–20]. However, due to the contradiction of the required high deposition temperature of VAN thin films and the low melting point of the flexible polymer substrates, flexible VAN has not been widely achieved, which hinders its further applications in flexible devices [21–23]. Recently, mica has been employed to realize flexible functional oxide thin

films because of its high melting point (1300 °C) and flexible nature after being cleaved into ultrathin form. Various epitaxial oxide thin films have been successfully demonstrated on flexible mica, such as CoFe_2O_4 (CFO) [24], $\text{La}_{0.67}\text{Sr}_{0.33}\text{MnO}_3$ (LSMO) [25], VO_2 [26], $\text{Pb}(\text{Zr}, \text{Ti})\text{O}_3$ (PZT) [27], SrRuO_3 (SRO) [28] and so forth. However, very limited attempts have been conducted to integrate VANs on mica [21–23], possibly due to its complicated growth mechanism with two phases being simultaneously involved during its growth.

Here, in this work, LSMO: CeO_2 (LC) nanocomposite thin films have been deposited on mica with or without a buffer layer, and BaTiO_3 (BTO) has been selected as the buffer because of its high epitaxial quality on mica [28]. Therefore, the introduction of BTO buffer might improve the quality of the LC film and consequently tailor its physical properties. LC has been demonstrated on STO with a typical VAN nanostructure, which presents a tailorable LFMP property by tuning the phase composition [29]. Furthermore, the LC system can even be grown into a 3D nanocomposite form, which shows an enhanced LFMR effect through film architecture design [13,30]. Therefore, we selected this well-studied nanocomposite system as a model to explore the feasibility of integrating VANs on flexible mica. The magnetic and LFMR properties of LC/mica and LC/BTO/mica have been investigated and compared. This work demonstrates the feasibility of fabricating flexible VAN thin films via mica integration, which lays the foundation for their future applications in flexible devices.

2. Results and Discussion

The LSMO- CeO_2 nanocomposite films were grown on mica and BTO-buffered mica using pulsed laser deposition (PLD) with a KrF excimer laser ($\lambda = 248$ nm). Before deposition, the chamber was vacuumed to a base pressure lower than 1.0×10^{-6} mbar. During deposition, the deposition conditions were as below: deposition temperature of 750 °C, oxygen pressure of 200 mTorr and laser frequency of 5 Hz. After deposition, the chamber was cooled down at a cooling rate of 10 °C/min under an oxygen pressure of 266 mbar. First, standard θ - 2θ XRD scans of LC nanocomposite thin films on mica with (LC/BTO/mica) or without (LC/mica) buffer layer were carried out and are shown in Figure 1. For LC/BTO/mica (blue line), only the BTO (111) peak was observed for the buffer layer, which illustrates the high quality of the buffer and is consistent with the reported BTO buffer for the growth of LSMO and SRO thin films [28,31]. For the LC layer, only CeO_2 (002) and LSMO (111) peaks existed, which indicate the textured growth of both phases on BTO-buffered mica. Furthermore, the lattice parameters of the two phases can be calculated to be $d_{\text{CeO}_2(200)} = 2.72$ Å and $d_{\text{LSMO}(111)} = 2.22$ Å, which correspond to 0.74% ($d_{\text{bulk CeO}_2(200)} = 2.706$ Å) tensile strain and -0.45% ($d_{\text{bulk LSMO}(111)} = 2.24$ Å) compressive strain in out-of-plane directions for CeO_2 and LSMO, respectively. For LC/mica (red line), only CeO_2 (111) and LSMO (llo) peaks were observed, which suggests the textured growth of both phases directly on mica. However, the growth orientations of CeO_2 and LSMO are different while being integrated on BTO/mica or mica. For the LC/mica sample, the substrate clamping effect played a non-critical role in film growth; therefore, CeO_2 and LSMO favor the (111) and (llo) growth directions with the lowest surface energy [32]. As reported previously, both LSMO (llo) and ($00l$) appeared while being directly grown on mica [25]. The incorporation of CeO_2 phase could stabilize the phase to grow along the (llo) direction. Furthermore, in LC/mica, $d_{\text{CeO}_2(111)}$ and $d_{\text{LSMO}(110)}$ could be estimated to be 3.15 Å and 2.73 Å, which correspond to 0.94% ($d_{\text{bulk CeO}_2(111)} = 3.124$ Å) tensile strain and -0.36% ($d_{\text{bulk LSMO}(110)} = 2.74$ Å) compressive strain in the out-of-plane direction for CeO_2 and LSMO, respectively. Such a strain could play an important role in the physical properties of the nanocomposite thin film, which will be discussed in a later section. Other than the peaks from the films, there are mica ($00l$) peaks marked by “#”. It is also worth noting that extra peaks exist, which are from the holder rather than the samples.

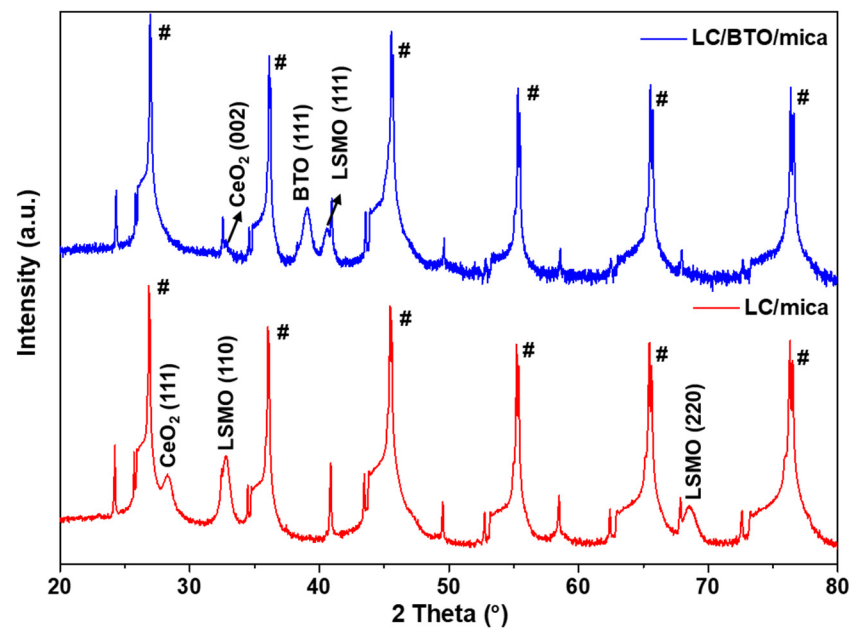


Figure 1. Standard θ - 2θ XRD scans of LC/BTO/mica and LC/mica samples, “#” corresponds to the mica (00 l) peaks.

We then investigated the microstructure of the LC nanocomposite thin films. Atomic force microscopy (AFM) was employed to explore the surface morphology of the LC/mica and LC/BTO/mica samples, as shown in Figures 2a and 2b, respectively.

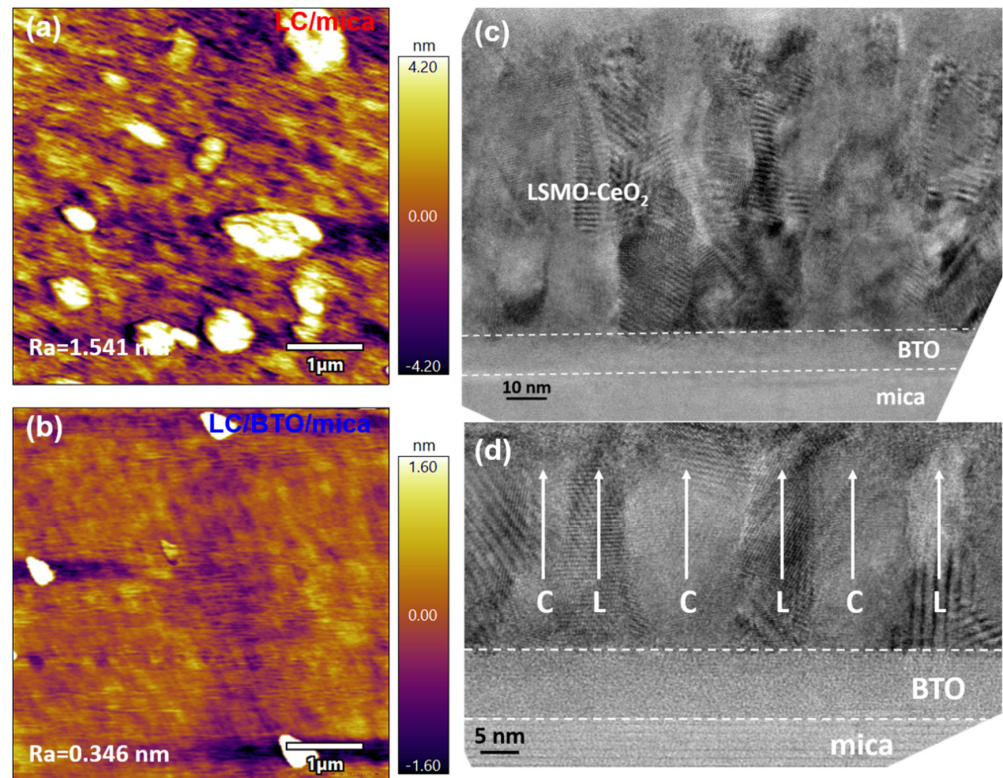


Figure 2. AFM images of (a) LC/mica and (b) LC/BTO/mica to show the surface morphology; (c) low-mag and (d) medium-mag TEM images of the LC/BTO/mica sample.

The LC/mica sample exhibits a relatively rough surface with a surface roughness of 1.541 nm, and a large amount of particles could be observed on the film’s surface.

The LC/BTO/mica film presents a much smoother surface with a surface roughness of 0.346 nm, and very few particles exist on the film's surface, which indicates that the buffer layer could provide an ideal platform for nanocomposite growth. To further explore the cross-sectional view of the LC/BTO/mica sample, transmittance electron microscopy (TEM) was conducted, as shown in Figure 2c. The thicknesses of the BTO and LC layers can be identified as ~ 10 nm and ~ 75 nm, respectively, while a clean LC/BTO heterointerface was presented. By focusing on the local area exhibited in Figure 2d, a typical VAN structure of alternate growth of CeO_2 and LSMO phases was observed, which confirms the successful integration of LC VAN thin film on mica.

Next, we explored the magnetic properties of LC/mica and LC/BTO/mica samples. Figure 3a presents the magnetic hysteresis loops (M-H) measured at 10 K under an out-of-plane (OP, perpendicular to the film surface) field (-1 T to 1 T). As is seen, the saturation magnetization (M_s) of LC/mica (~ 295 emu/cm³) is higher than LC/BTO/mica (~ 202 emu/cm³). Considering CeO_2 is a nonmagnetic material, LSMO is the origin of the magnetic performance in this case. The M_s difference could be attributed to the different strain condition in the LSMO phase. Specifically, LSMO in LC/mica obtains smaller OP strain (corresponds to larger in-plane strain), which could shorten the Mn-O-Mn bond length and enhance the double-exchange interaction between Mn^{3+} and Mn^{4+} ions, and consequently increase the M_s value of LSMO [33,34]. On the other hand, the coercivity (H_c) value of LSMO in LC/BTO/mica shows a larger value of ~ 1150 Oe than ~ 300 Oe for the LC/mica sample (shown in Figure 3b), which could be due to multiple aspects, such as the magnetic anisotropy in LSMO [35], the amount of grain boundaries [36], and the strain state [37]. Specifically, the LSMO (111) phase exists in LC/BTO/mica with larger OP strain, while the LSMO (110) phase appears in LC/mica with a smaller OP strain. In addition, more grain boundaries (smaller grain size) could be observed in LC/BTO/mica, which could act as domain-pinning sites to hinder magnetization reversal and hence enhance the H_c value.

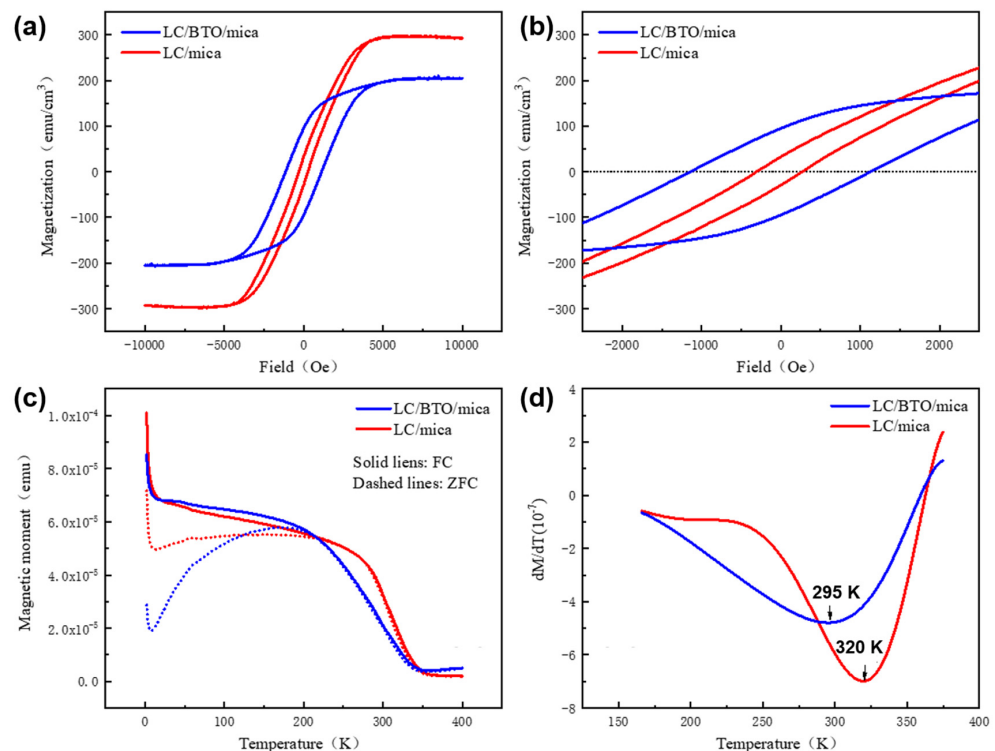


Figure 3. (a) M–H curves of LC/BTO/mica and LC/mica samples, with (b) the local area to determine H_c ; (c) M–T measurements under FC and ZFC conditions; (d) dM/dT curves to determine the Curie temperature.

Temperature-dependent magnetization ($M-T$, 5–400 K) measurements under field cooling (FC, applied magnetic field of 100 Oe) and zero-field cooling (ZFC) were also performed and are plotted in Figure 3c. For both samples, the magnetization monotonically decreases as temperature increases under FC, while it increases gradually to a maximum value (blocking temperature: T_B) before decreasing monotonically with increasing temperature under ZFC. Furthermore, a bifurcation between the ZFC and FC curves was observed at ~ 210 K, termed as irreversibility temperature (T_{irr}). To determine the Curie temperature (T_C) of the samples, dM/dT , dependent on the temperature curves, is plotted in Figure 3d, and T_C values of 295 K and 320 K can be identified for LC/BTO/mica and LC/mica, respectively. The T_C values in LC thin films are lower than their bulk value of 370 K [38]; such a reduction could be ascribed to the suppressed double-exchange coupling by the disordered phase and the large amount of grain boundaries [39]. Furthermore, the OP compressive strain of LSMO in LC nanocomposite thin films could lead to an increase in the Mn-O-Mn bond length, inhibiting e_g electron hopping and thus reducing T_C [40].

To resolve the transport and magnetoresistance (MR) properties in the flexible LC thin films, the temperature-dependent resistance ($R-T$) curves under zero field (R_0-T : solid lines) or 1 T field (R_H-T : dashed lines) are shown and compared in Figure 4a. It should be noted that the metal-insulator transition temperature (T_{MI}) of LC/BTO/mica (red line) is lower than LC/mica (pink line), which could be attributed to a smaller domain size and increased disorder in the former [41]. The MR values were calculated based on R_0-T and R_H-T curves using the equation $MR = R_0 - R_H/R_0 \times 100\%$, and the MR- T curves are presented in Figure 4b. It is evident that both films show large MR values at low temperature, e.g., $\sim 38\%$ for LC/BTO/mica and $\sim 34\%$ for LC/mica at 20 K, which is higher than the same LC films on single-crystal STO [29,42], as well as other perovskite-based bulk composites and nanocomposite thin films [41,43]. Lastly, considering the practical application of the flexible LC films, the samples were mechanically bent 500 times and the same measurements were carried out, as shown in Figure 4a for the $R-T$ curves and Figure 4b for the derived MR- T curves. The bending condition was realized by attaching the samples on a curved plastic mode (radius of ~ 14 mm). Apparently, the films exhibited a similar trend and T_{MI} after being bent 500 times, and the MR values were also maintained along all measured temperatures. Overall, both LC/BTO/mica and LC/mica films present excellent LFMR effects with high mechanical stability, which could be promising for future flexible device integration.

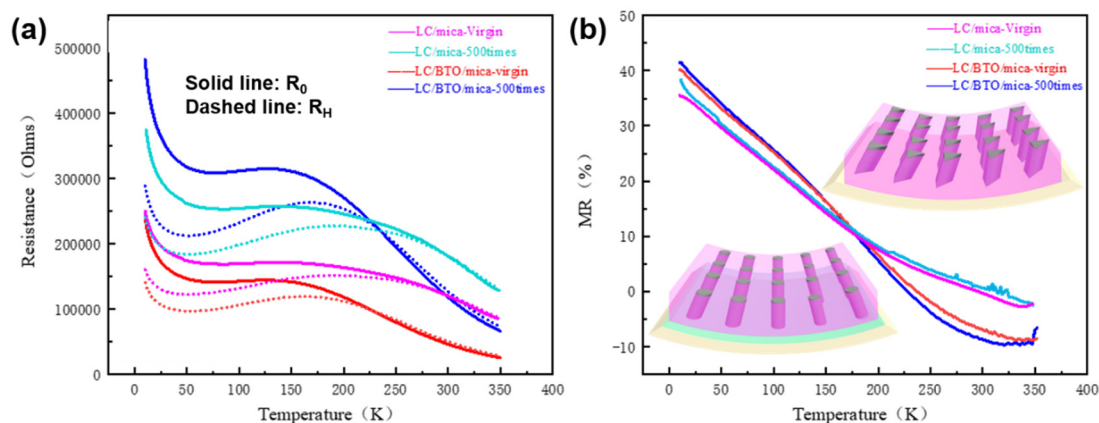


Figure 4. (a) The temperature-dependent resistance ($R-T$) curves under zero field (R_0-T : solid lines) or 1 T field (R_H-T : dashed lines) for LC/BTO/mica and LC/mica with or without bending; (b) MR- T curves derived from the $R-T$ data.

3. Conclusions

LSMO-CeO₂ nanocomposite thin films have been deposited on mica substrates with or without a BTO buffer layer. Both films present high texture growth, and LSMO (111)

and CeO₂ (002) phases exist in LC/BTO/mica while LC/mica contains LSMO (110) and CeO₂ (111) phases, without any impurity phases. Different magnetic, transport and magnetoresistance properties have been explored for LC/BTO/mica and LC/mica, e.g., higher saturation magnetization, smaller coercivity and higher metal-insulator transition temperature were determined in LC/mica. Both films show high low-field magnetoresistance values at a low temperature. Furthermore, the flexible LC nanocomposite thin films present excellent mechanical stability after bending.

4. Experimental

Target preparation: The LSMO-CeO₂ with a molar ratio of 1:1 composite target was prepared via a conventional ceramic sintering process. Specifically, a stoichiometric mixture of La₂O₃, MnO₂, SrCO₃ and CeO₂ powders was mixed, ground and pressed into a disk (1 inch diameter), and then the disk was annealed at 1300 °C in air for 12 h. A commercial BTO target was used for the deposition of the BTO buffer layer.

Thin-film deposition: The LSMO-CeO₂ nanocomposite films were grown on mica and BTO-buffered mica using pulsed laser deposition (PLD) with a KrF excimer laser ($\lambda = 248$ nm). Before deposition, the chamber was vacuumed to a base pressure lower than 1.0×10^{-6} mbar. During deposition, the deposition conditions were as below: deposition temperature of 750 °C, oxygen pressure of 200 mTorr and laser frequency of 5 Hz. After deposition, the chamber was cooled down at a cooling rate of 10 °C/min under an oxygen pressure of 266 mbar.

Property characterizations: The crystal structure and microstructure of the films were characterized by X-ray diffraction (XRD) (Panalytical X'Pert X-ray diffractometer, Malvern Panalytical Ltd., Malvern, UK) atomic force microscopy (AFM) (CSPM5500, Being Nano-Instruments, Beijing, China) and transmission electron microscopy (TEM) (FEI Tecnai F30, FEI Company, Hillsboro, USA). Magnetic hysteresis (M–H) loops and temperature dependence of magnetization (M–T) were measured using a SQUID magnetometer (MPMS: Quantum Design). Resistance dependent on temperature (R–T) measurement was carried out using a physical property measurement system (PPMS: Quantum Design).

Author Contributions: Conceptualization, J.H.; methodology, H.T., X.Z. and F.W.; formal analysis, H.T., X.Z. and A.A.; resources, J.J. and J.H.; writing—original draft preparation, H.T., A.A. and F.W.; writing—review and editing, J.J. and J.H.; supervision, J.J. and J.H.; funding acquisition, A.A. and J.H. All authors have read and agreed to the published version of the manuscript.

Funding: J.H. acknowledges support from the Shenzhen Science and Technology Program (JCYJ20210324133610028) and Guangdong Basic and Applied Basic Research Foundation (2023A1515012594). A.A. acknowledges Researchers Supporting Project number (RSP2023R304), King Saud University, Riyadh, Saudi Arabia.

Data Availability Statement: Data is contained within the article.

Conflicts of Interest: The authors declare no conflict of interest.

References

1. Lorenz, M.; Rao, M.R.; Venkatesan, T.; Fortunato, E.; Barquinha, P.; Branquinho, R.; Salgueiro, D.; Martins, R.; Carlos, E.; Liu, A.; et al. The 2016 oxide electronic materials and oxide interfaces roadmap. *J. Phys. D Appl. Phys.* **2016**, *49*, 433001. [[CrossRef](#)]
2. Huang, J.; MacManus-Driscoll, J.L.; Wang, H. New epitaxy paradigm in epitaxial self-assembled oxide vertically aligned nanocomposite thin films. *J. Mater. Res.* **2017**, *32*, 4054–4066. [[CrossRef](#)]
3. MacManus-Driscoll, J.L.; Zerrer, P.; Wang, H.; Yang, H.; Yoon, J.; Fouchet, A.; Yu, R.; Blamire, M.G.; Jia, Q. Strain control and spontaneous phase ordering in vertical nanocomposite heteroepitaxial thin films. *Nat. Mater.* **2008**, *7*, 314–320. [[CrossRef](#)] [[PubMed](#)]
4. Huang, J.; Li, W.; Yang, H.; MacManus, J.L. Tailoring physical functionalities of complex oxides by vertically aligned nanocomposite thin-film design. *MRS Bull.* **2021**, *46*, 159–167. [[CrossRef](#)]
5. Wang, J.; Neaton, J.B.; Zheng, H.; Nagarajan, V.; Ogale, S.B.; Liu, B.; Viehland, D.; Vaithyanathan, V.; Schlom, D.G.; Waghmare, U.V.; et al. Epitaxial BiFeO₃ multiferroic thin film heterostructures. *Science* **2003**, *299*, 1719–1722. [[CrossRef](#)]
6. Wang, N.; Luo, X.; Han, L.; Zhang, Z.; Zhang, R.; Olin, H.; Yang, Y. Structure, performance, and application of BiFeO₃ nanomaterials. *Nano-Micro Lett.* **2020**, *12*, 81. [[CrossRef](#)] [[PubMed](#)]

7. Kimura, T.; Goto, T.; Shintani, H.; Ishizaka, K.; Arima, T.; Tokura, Y. Magnetic control of ferroelectric polarization. *Nature* **2003**, *426*, 55–58. [[CrossRef](#)]
8. Hu, N.; Lu, C.; Xia, Z.; Xiong, R.; Fang, P.; Shi, J.; Liu, J. Multiferroicity and magnetoelectric coupling in TbMnO₃ thin films. *ACS Appl. Mater. Interfaces* **2015**, *7*, 26603–26607. [[CrossRef](#)]
9. Zheng, H.; Wang, J.; Lofand, S.E.; Ma, Z.; Mohaddes-Ardabili, L.; Zhao, T.; Salamanca-Riba, L.; Shinde, S.R.; Ogale, S.B.; Bai, F.; et al. Multiferroic BaTiO₃-CoFe₂O₄ nanostructures. *Science* **2004**, *303*, 661–663. [[CrossRef](#)]
10. Wang, H.; Li, L.; Huang, J.; Gao, X.; Sun, X.; Wang, H. Multiferroic vertically aligned nanocomposite with CoFe₂O₄ nanocones embedded in layered Bi₂WO₆ matrix. *Mater. Res. Lett.* **2019**, *7*, 418–425. [[CrossRef](#)]
11. Lee, O.; Harrington, S.A.; Kursumovic, A.; Defay, E.; Wang, H.; Bi, Z.; Tsai, C.; Yan, L.; Jia, Q.; MacManus-Driscoll, J.L. Extremely high tunability and low loss in nanoscaffold ferroelectric films. *Nano Lett.* **2012**, *12*, 4311–4317. [[CrossRef](#)] [[PubMed](#)]
12. Huang, J.; Zhang, D.; Liu, J.; Wang, H. Freestanding La_{0.7}Sr_{0.3}MnO₃: NiO vertically aligned nanocomposite thin films for flexible perpendicular interfacial exchange coupling. *Mater. Res. Lett.* **2022**, *10*, 287–294. [[CrossRef](#)]
13. Sun, X.; Huang, J.; Jian, J.; Fan, M.; Wang, H.; Li, Q.; MacManus-Driscoll, J.L.; Lu, P.; Zhang, X.; Wang, H. Three-dimensional strain engineering in epitaxial vertically aligned nanocomposite thin films with tunable magnetotransport properties. *Mater. Horiz.* **2018**, *5*, 536–544. [[CrossRef](#)]
14. Ma, W.; Kim, J.; Tsvetkov, N.; Daio, T.; Kuru, Y.; Cai, Z.; Chen, Y.; Sasaki, K.; Tuller, H.L.; Yildiz, B. Vertically aligned nanocomposite La_{0.8}Sr_{0.2}CoO₃/(La_{0.5}Sr_{0.5})₂CoO₄ cathodes—Electronic structure, surface chemistry and oxygen reduction kinetics. *J. Mater. Chem. A* **2015**, *3*, 207–219. [[CrossRef](#)]
15. Huang, J.; Wang, H.; Qi, Z.; Lu, P.; Zhang, D.; Zhang, B.; He, Z.; Wang, H. Multifunctional Metal–Oxide Nanocomposite Thin Film with Plasmonic Au Nanopillars Embedded in Magnetic La_{0.67}Sr_{0.33}MnO₃ Matrix. *Nano Lett.* **2021**, *21*, 1032–1039. [[CrossRef](#)] [[PubMed](#)]
16. Huang, J.; Wang, X.; Hogan, N.; Wu, S.; Lu, P.; Fan, Z.; Dai, Y.; Zeng, B.; Starko-Bowes, R.; Jian, J.; et al. Nanoscale artificial plasmonic lattice in self-assembled vertically aligned nitride–metal hybrid metamaterials. *Adv. Sci.* **2018**, *6*, 1800416. [[CrossRef](#)]
17. Huang, J.; Phuah, X.L.; McClintock, L.M.; Padmanabhan, P.; Vikrant, K.S.N.; Wang, H.; Zhang, D.; Wang, H.; Lu, P.; Gao, X.; et al. Core-shell metallic alloy nanopillars-in-dielectric hybrid metamaterials with magneto-plasmonic coupling. *Mater. Today* **2021**, *51*, 39–47. [[CrossRef](#)]
18. Huang, J.; Gellatly, A.; Kauffmann, A.; Sun, X.; Wang, H. Exchange bias effect along vertical interfaces in La_{0.7}Sr_{0.3}MnO₃: NiO vertically aligned nanocomposite thin films integrated on silicon substrates. *Cryst. Growth Des.* **2018**, *18*, 4388–4394. [[CrossRef](#)]
19. Tian, H.; Wang, G.; Wang, F.; Jiang, C.; Huang, J. Si integration of La_{0.7}Sr_{0.3}MnO₃: BiFeO₃ nanocomposite thin films with strong exchange bias coupling. *Appl. Phys. Lett.* **2022**, *121*, 022403. [[CrossRef](#)]
20. Zhang, W.; Chen, A.; Khatkhatay, F.; Tsai, C.F.; Su, Q.; Jiao, L.; Zhang, X.; Wang, H. Integration of self-assembled vertically aligned nanocomposite (La_{0.7}Sr_{0.3}MnO₃)_{1-x}:(ZnO)_x thin films on silicon substrates. *ACS Appl. Mater. Interfaces* **2013**, *5*, 3995–3999. [[CrossRef](#)]
21. Zhang, X.; Yang, H.; Wang, G.; Zhang, Y.; Huang, J. Flexible La_{0.67}Sr_{0.33}MnO₃: ZnO Nanocomposite Thin Films Integrated on Mica. *Front. Mater.* **2022**, *9*, 913326. [[CrossRef](#)]
22. Amrillah, T.; Bitla, Y.; Shin, K.; Yang, T.; Hsieh, Y.H.; Chiou, Y.Y.; Liu, H.J.; Do, T.H.; Su, D.; Chen, Y.C.; et al. Flexible multiferroic bulk heterojunction with giant magnetoelectric coupling via van der Waals epitaxy. *ACS Nano* **2017**, *11*, 6122–6130. [[CrossRef](#)] [[PubMed](#)]
23. Huang, J.; Wang, H.; Wang, X.; Gao, X.; Liu, J.; Wang, H. Exchange bias in a La_{0.67}Sr_{0.33}MnO₃/NiO heterointerface integrated on a flexible mica substrate. *ACS Appl. Mater. Interfaces* **2020**, *12*, 39920–39925. [[CrossRef](#)] [[PubMed](#)]
24. Liu, H.J.; Wang, C.K.; Su, D.; Amrillah, T.; Hsieh, Y.H.; Wu, K.H.; Chen, Y.C.; Juang, J.Y.; Eng, L.M.; Jen, S.U.; et al. Flexible heteroepitaxy of CoFe₂O₄/muscovite bimorph with large magnetostriction. *ACS Appl. Mater. Interfaces* **2017**, *9*, 7297–7304. [[CrossRef](#)] [[PubMed](#)]
25. Ye, L.; Zhang, D.; Lu, J.; Xu, S.; Xu, R.; Fan, J.; Tang, R.; Wang, H.; Guo, H.; Li, W.; et al. Epitaxial (110)-oriented La_{0.7}Sr_{0.3}MnO₃ film directly on flexible mica substrate. *J. Phys. D Appl. Phys.* **2022**, *55*, 224002. [[CrossRef](#)]
26. Li, C.I.; Lin, J.C.; Liu, H.J.; Chu, M.W.; Chen, H.W.; Ma, C.H.; Tsai, C.Y.; Huang, H.W.; Lin, H.J.; Liu, H.L.; et al. Van der Waal epitaxy of flexible and transparent VO₂ film on muscovite. *Chem. Mater.* **2016**, *28*, 3914–3919. [[CrossRef](#)]
27. Jiang, J.; Bitla, Y.; Huang, C.W.; Do, T.H.; Liu, H.J.; Hsieh, Y.H.; Ma, C.H.; Jang, C.Y.; Lai, Y.H.; Chiu, P.W.; et al. Flexible ferroelectric element based on van der Waals heteroepitaxy. *Sci. Adv.* **2017**, *3*, e1700121. [[CrossRef](#)]
28. Liu, J.; Feng, Y.; Tang, R.; Zhao, R.; Gao, J.; Shi, D.; Yang, H. Flexible Electronics: Mechanically Tunable Magnetic Properties of Flexible SrRuO₃ Epitaxial Thin Films on Mica Substrates. *Adv. Electron. Mater.* **2018**, *4*, 1700522. [[CrossRef](#)]
29. Fan, M.; Zhang, W.; Khatkhatay, F.; Li, L.; Wang, H. Enhanced tunable magnetoresistance properties over a wide temperature range in epitaxial (La_{0.7}Sr_{0.3}MnO₃)_{1-x}:(CeO₂)_x nanocomposites. *J. Appl. Phys.* **2015**, *118*, 065302. [[CrossRef](#)]
30. Sun, X.; Li, Q.; Huang, J.; Fan, M.; Rutherford, B.X.; Paldi, R.L.; Jian, J.; Zhang, X.; Wang, H. Strain-driven nanodumbbell structure and enhanced physical properties in hybrid vertically aligned nanocomposite thin films. *Appl. Mater. Today* **2019**, *16*, 204–212. [[CrossRef](#)]
31. Fan, J.; Xie, Y.; Qian, F.; Ji, Y.; Hu, D.; Tang, R.; Liu, W.; Zhang, L.; Tong, W.; Ma, C.; et al. Isotropic magnetoresistance and enhancement of ferromagnetism through repetitious bending moments in flexible perovskite manganite thin film. *J. Alloys Compd.* **2019**, *806*, 753–760. [[CrossRef](#)]

32. Skorodumova, N.V.; Baudin, M.; Hermansson, K. Surface properties of CeO₂ from first principles. *Phys. Rev. B* **2004**, *69*, 075401. [[CrossRef](#)]
33. Liu, Y.P.; Du, Y.S.; Zhang, M.; Yan, H.; Wang, Y.Y. Effect of internal strain on magnetic properties of La_{0.7}Sr_{0.3}MnO₃ films. *Vacuum* **2007**, *81*, 826–829. [[CrossRef](#)]
34. Praus, R.B.; Gross, G.M.; Razavi, F.S.; Habermeier, H.-U. Effects of strain on the properties of La_{0.67}Ca_{0.33}MnO₃ thin films. *J. Magn. Magn. Mater.* **2000**, *211*, 41–46. [[CrossRef](#)]
35. Mathews, M.; Postma, F.M.; Lodder, J.C.; Jansen, R.; Rijnders, G.; Blank, D.H.A. Step-induced uniaxial magnetic anisotropy of La_{0.67}Sr_{0.33}MnO₃ thin films. *Appl. Phys. Lett.* **2005**, *87*, 242507. [[CrossRef](#)]
36. Pardavi-Horvath, M. Coercivity of epitaxial magnetic garnet crystals. *IEEE Trans. Magn.* **1985**, *21*, 1694–1699. [[CrossRef](#)]
37. Lu, Z.; Liu, J.; Feng, J.; Zheng, X.; Yang, L.; Ge, C.; Jin, K.; Wang, Z.; Li, R. Synthesis of single-crystal La_{0.67}Sr_{0.33}MnO₃ freestanding films with different crystal-orientation. *APL Mater.* **2020**, *8*, 051105. [[CrossRef](#)]
38. Urushibara, A.; Moritomo, Y.; Arima, T.; Asamitsu, A.; Kido, G.; Tokura, Y. Insulator-metal transition and giant magnetoresistance in La_{1-x}Sr_xMnO₃. *Phys. Rev. B* **1995**, *51*, 14103. [[CrossRef](#)]
39. Rivadulla, F.; Otero-Leal, M.; Espinosa, A.; de Andres, A.; Ramos, C.; Rivas, J.; Goodenough, J.B. Suppression of ferromagnetic double exchange by vibronic phase segregation. *Phys. Rev. Lett.* **2006**, *96*, 016402. [[CrossRef](#)]
40. Rao, R.A.; Lavric, D.; Nath, T.K.; Eom, C.B.; Wu, L.; Tsui, F. Three-dimensional strain states and crystallographic domain structures of epitaxial colossal magnetoresistive La_{0.8}Ca_{0.2}MnO₃ thin films. *Appl. Phys. Lett.* **1998**, *73*, 3294–3296. [[CrossRef](#)]
41. Kang, B.S.; Wang, H.; MacManus-Driscoll, J.L.; Li, Y.; Jia, Q.; Mihut, I.; Betts, J.B. Low field magnetotransport properties of (La_{0.7}Sr_{0.3}MnO₃)_{0.5}(ZnO)_{0.5} nanocomposite films. *Appl. Phys. Lett.* **2006**, *88*, 192514. [[CrossRef](#)]
42. Chen, A.; Bi, Z.; Hazariwala, H.; Zhang, X.; Su, Q.; Chen, L.; Jia, Q.; MacManus-Driscoll, J.L.; Wang, H. Microstructure, magnetic, and low-field magnetotransport properties of self-assembled (La_{0.7}Sr_{0.3}MnO₃)_{0.5}(ZnO)_{0.5} vertically aligned nanocomposite thin films. *Nanotechnology* **2011**, *22*, 315712. [[CrossRef](#)]
43. Xiong, C.; Zeng, Y.; Xiong, Y.; Zhang, J.; Pi, Y.; Zhang, L.; Xiong, J.; Cheng, X.; Wei, F.; Li, L. Low-field transport properties of (1-x)La_{0.7}Ca_{0.2}Sr_{0.1}MnO₃+x(ZnO) composites. *Phys. B* **2008**, *403*, 3266–3270. [[CrossRef](#)]

Disclaimer/Publisher's Note: The statements, opinions and data contained in all publications are solely those of the individual author(s) and contributor(s) and not of MDPI and/or the editor(s). MDPI and/or the editor(s) disclaim responsibility for any injury to people or property resulting from any ideas, methods, instructions or products referred to in the content.